Chinese Chemical Letters 36 (2025) 110765

Contents lists available at ScienceDirect

Chinese Chemical Letters

journal homepage: www.elsevier.com/locate/cclet

Supramolecular-orchestrated carrier-free chemodynamic synergists with augmented oxidative damage for potentiated cancer therapy

Xiaoyi Meng[a,1], Xinyue Sun[d,1], Zhaogang Sun[c], Yue Cheng[a,*], Yong Wang[a], Jun Ye[e,*], Yin Xiao[b,*], Hongqian Chu[c,*]

[a] Department of Chemistry, School of Science, Tianjin University, Tianjin 300072, China
[b] Department of Fine Chemical Engineering, School of Chemical Engineering and Technology, Tianjin University, Tianjin 300072, China
[c] Translational Medicine Center, Beijing Chest Hospital, Capital Medical University/Beijing Tuberculosis and Thoracic Tumor Research Institute, Beijing 101149, China
[d] State Key Laboratory of Quality Research in Chinese Medicine, Institute of Chinese Medical Sciences, University of Macau, Macau SAR 999078, China
[e] State Key Laboratory of Bioactive Substance and Function of Natural Medicines, Institute of Materia Medica, Chinese Academy of Medical Sciences & Peking Union Medical College, Beijing 100050, China

ARTICLE INFO

Article history:
Received 20 October 2024
Revised 12 December 2024
Accepted 13 December 2024
Available online 13 December 2024

Keywords:
Supramolecular orchestration
Carrier-free delivery
MTH1 inhibition
Chemodynamic therapy
Oxidative damage

ABSTRACT

Metal ions trigger Fenton/Fenton-like reactions, generating highly toxic hydroxyl radicals (·OH) for chemodynamic therapy (CDT), which is crucial in inducing lethal oxidative DNA damage and subsequent cell apoptosis. However, tumor cells can counteract this damage through repair pathways, particularly MutT homolog 1 (MTH1) protein attenuation of oxidative DNA damage. Suppression of MTH1 can enhance CDT efficacy, therefore, orderly integrating Fenton/Fenton-like agents with an MTH1 inhibitor is expected to significantly augment CDT effectiveness. Carrier-free CuTH@CD, self-assembled through the supramolecular orchestration of γ-cyclodextrin (γ-CD) with Cu^{2+} and the MTH1 inhibitor TH588, effectively overcoming tumor resistance by greatly amplifying oxidative damage capability. Without additional carriers and mediated by multiple supramolecular regulatory effects, CuTH@CD enables high drug loading content, stability, and uniform size distribution. Upon internalization by tumor cells, CuTH@CD invalidates repair pathways through Cu^{2+}-mediated glutathione (GSH) depletion and TH588-mediated MTH1 inhibition. Meanwhile, both generated Cu^{+} ions and existing ones within the nanoassembly initiate a Fenton-like reaction, leading to the accumulation of ·OH. This strategy enhances CDT efficiency with minimal side effects, improving oxidative damage potency and advancing self-delivery nanoplatforms for developing effective chemodynamic tumor therapies.

Reactive oxygen species (ROS), by-products of aerobic respiration, act as potent oxidants that induce oxidative stress at high concentrations within tumor cells, resulting in DNA and protein damage [1,2]. ROS are thus attractive therapeutic targets for cancer treatment, capable of triggering apoptosis and necrosis to some extent [3–5]. Recent advancements in nanotechnology have facilitated dynamic therapy (DT) as a promising approach for tumor treatment, encompassing chemodynamic therapy (CDT) [6–10], photodynamic therapy (PDT) [11,12], and sonodynamic therapy (SDT) [13,14]. These therapies locally generate cytotoxic ROS, effectively eradicating tumor cells [15,16]. Among these, CDT stands out for its direct induction of metal ion-mediated Fenton/Fenton-like reactions within tumors, generating ·OH without external energy input, ensuring high specificity [17,18], safety [19,20], and non-invasiveness [21,22]. There is considerable evidence that the accumulation of ROS effectively amplifies oxidative damage, thereby enhancing susceptibility to cellular apoptosis and potentially inhibiting oncogenic characteristics, thereby impeding tumor progression [23–26]. Therefore, developing an integrated system to augment ROS accumulation during CDT is crucial.

Elevated levels of ROS can oxidize the free deoxynucleoside triphosphate (dNTP) pool, generating 8-oxo-7,8-dihydroguanine (8-oxo-dG) [27], which can be incorporated into genomic DNA and cause mismatches [28]. The MutT homolog 1 (MTH1, a self-protecting functional protein) protein enzymatically hydrolyzes the triphosphate form of 8-oxo-dG into its monophosphate form

* Corresponding authors.
E-mail addresses: chengyue90@tju.edu.cn (Y. Cheng), yelinghao@imm.ac.cn (J. Ye), xiaoyin@tju.edu.cn (Y. Xiao), chuhongqian@bjxkyy.cn (H. Chu).
[1] These authors contributed equally to this work.

https://doi.org/10.1016/j.cclet.2024.110765
1001-8417/

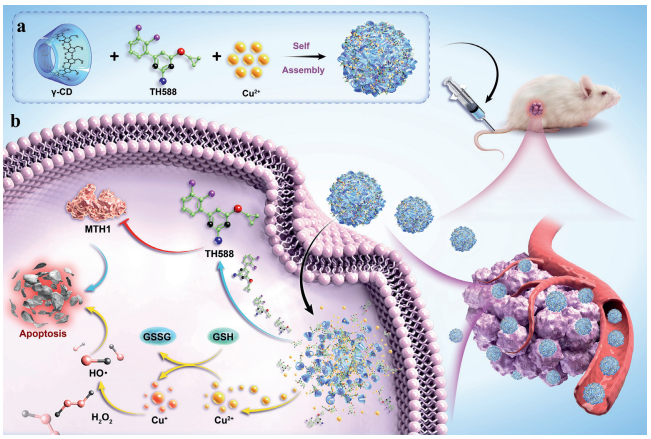

Scheme 1. (a) Schematic illustration of the fabrication process of CuTH@CD NPs. (b) The therapeutic mechanism scheme illustrating the amplification of oxidative damage *in vivo* through MTH1 inhibition, GSH consumption, and ·OH production.

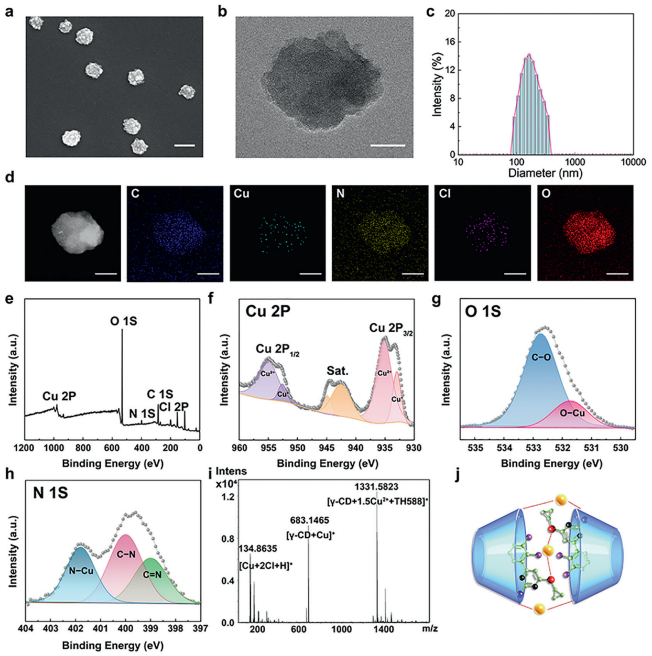

Fig. 1. Characterization of CuTH@CD. (a) SEM and (b) TEM images of CuTH@CD. Scale bar: 200 nm (SEM) and 50 nm (TEM). (c) Hydrodynamic diameter of CuTH@CD. (d) Elemental mapping images of a single CuTH@CD. Scale bar: 50 nm. (e) XPS survey spectrum of CuTH@CD. (f) Cu 2p, (g) O 1s and (h) N 1s region high-resolution XPS spectrum. (i) ESI-MS of CuTH@CD. (j) Schematic diagram of reasonable structure of CuTH@CD.

in vivo [29], thereby preventing the incorporation of oxidized nucleotides into DNA and suppressing DNA damage [30–32]. MTH1 inhibitors like TH588 have been developed to promote DNA mismatches in tumor cells to amplify oxidative damage caused by ROS [33–36]. However, TH588 is commonly used in combination with PDT, which faces limitations due to the tumor hypoxia [37,38]. Moreover, TH588 and other drug molecules necessitate carriers for targeted delivery to tumor regions, often composed of degradable and poorly metabolized materials that may potentially induce systemic toxicity and immunogenicity when administered at higher concentrations [39,40]. Recently, carrier-free nanomedicines based on self-assembly have emerged as promising alternatives for enhancing tumor therapy efficacy [41,42]. These nanoassemblies exhibit high drug loading capacity [43,44], flexible preparation methods [45], and avoid carrier-induced toxicity and immunogenicity risks [46], making them ideal for co-delivering TH588 and CDT reagents to amplify ROS-mediated oxidative damage.

Herein, we present a smartly-designed CuTH@CD material to achieve the augmented ROS accumulation. This nanoplatform was synthesized through cyclodextrin-mediated self-assembly of Cu^{2+} and the MTH1 inhibitor TH588 (Scheme 1a). CuTH@CD achieves high drug loading content, stability, and uniform size distribution, effectively integrating potent Fenton-like agents with an MTH1 inhibitor to suppress ROS elimination and amplify oxidative damage during CDT. Upon internalization into tumor cells, CuTH@CD releases Cu^{2+} to deplete intracellular glutathione (GSH, an antioxidant) and preventing ROS scavenging. Simultaneously, Cu^{+} within the nanoassembly, along with newly generated Cu^{+} species, triggers a Fenton-like reaction, producing highly cytotoxic ·OH that enhances CDT efficacy. Additionally, TH588 inhibits the protective effect of MTH1, promoting apoptosis and further amplifying ROS-induced oxidative damage (Scheme 1b). This supramolecular-regulated self-assembly strategy of CuTH@CD maximizes ROS-induced oxidative damage while avoiding potential side effects associated with conventional carrier systems.

Maximizing therapeutic efficacy requires versatile nanoassemblies, and ensuring biosafety is a crucial aspect for their clinical translation. The synergistic combination of Cu^{2+} and the MTH1 inhibitor optimizes ROS oxidative damage, facilitated by the nitrogen atom in TH588 donating electrons to the unoccupied orbital of Cu, enabling effective coordination condition between TH588 and Cu^{2+}. However, achieving stable, uniform and well-dispersed nanoassemblies through a simple and efficient self-assembly process remains challenging. Encouragingly, γ-cyclodextrin (γ-CD), a biocompatible cyclic oligosaccharide, demonstrates its ability to form metal-organic complexes with divalent transition metal ions (Mn, Fe, Co, Ni, Cu, Zn) from the first subgroup [47–49]. The cavity inclusion and hydroxyl group coordination in γ-CD enable versatile supramolecular regulation, supported by its potent supramolecular templating effect in forming trimeric heteroaggregates [50]. In this study, we utilized the supramolecular template effect of γ-CD to incorporate it into the Cu^{2+}-TH588 system, forming a homogeneous trimeric heteroaggregate CuTH@CD *via* an ultrasound-assisted method, and characterized by scanning electron microscopy (SEM) and transmission electron microscopy (TEM), revealing a nearly spherical microstructure of approximately 130 nm diameter with excellent dispersibility (Figs. 1a and b, Fig. S1a in Supporting information). Without γ-CD modulation, nanoassembly aggregation was evident (Fig. S1b in Supporting information), highlighting its role in promoting the assembly of Cu^{2+} and TH588. This supramolecular templating effect facilitated trimeric heteroaggregate formation. Dynamic light scattering (DLS) analysis confirmed a hydrodynamic diameter of approximately 180 nm for CuTH@CD in solution (Fig. 1c, Fig. S2 in Supporting information), facilitating efficient enrichment at the tumor site through the enhanced permeability and retention (EPR) effect, thereby enhancing *in vivo* drug utilization.

Elemental mapping images confirmed the successful assembly of Cu^{2+}, TH588 and γ-CD with a uniform distribution of carbon (C), nitrogen (N), oxygen (O), chlorine (Cl) and copper (Cu) (Fig. 1d). X-ray photoelectron spectroscopy (XPS) analysis further substantiated the coexistence of these elements, consistent with the aforementioned results (Fig. 1e). As shown in Fig. 1f, Cu 2p XPS spectrum revealed distinct splitting in the excited state with Cu $2p_{1/2}$ composed of 68.3% Cu^{2+} (955.0 eV) and 31.7% Cu^{+} (952.6 eV), while Cu $2p_{3/2}$ composed of 69.3% Cu^{2+} (935.1 eV) and 30.7% Cu^{+} (933.0 eV). The ratio of peak areas between Cu^{2+} and Cu^{+} was approximately 2:1, indicating a significant abundance of Cu^{2+}, which exhibited high potential for redox reaction with GSH, further improving the ability to promote oxidative damage *via* Fenton-like re-

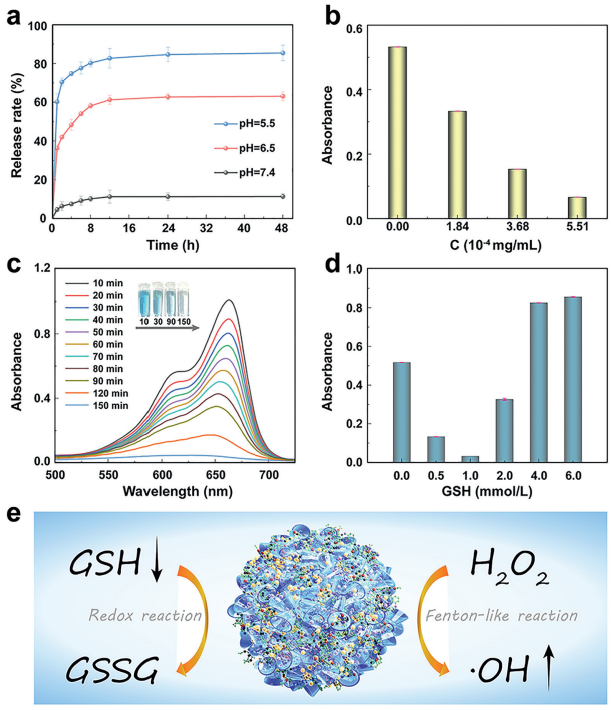

Fig. 2. (a) Cumulative release curves of TH588 in CuTH@CD in PBS solution with different pH values (7.4, 6.5, 5.5). (b) UV absorption spectra were analyzed for the catalytic consumption of 1.0 mmol/L GSH by varying concentrations of CuTH@CD. (c) Time-dependent UV absorption spectrum of MB catalyzed by CuTH@CD. (d) UV absorption spectroscopy of MB degradation catalyzed by Cu^{2+}/Cu^{+} at different GSH concentrations. (e) Schematic illustration of GSH consumption by Cu^{2+} and Cu^{+}-mediated ·OH generation. Data are presented as mean ± standard deviation (SD) ($n = 3$).

action. As shown in Fig. 1g, two oxygen characteristic peaks were observed at 532.7 and 531.7 eV respectively, representing C–O and O–Cu bonds. The nitrogen shifts spectrum displayed peaks at 401.8, 400.0 and 399.0 eV, assigned to N–Cu bondings along with C–N and C=N linkages (Fig. 1h). The Cu 2p, O 1s and N 1s shift spectra proved that Cu coordinated with N in TH588 and O in γ-CD, forming a stable complex. Electrospray ionization mass spectrometry (ESI-MS) revealed a univalent ion peak at about *m/z* 134 for $[Cu+2Cl+H]^{+}$, two divalent ion peaks at about *m/z* 683 and 1331 for $[\gamma\text{-CD}+Cu]^{2+}$ and $[\gamma\text{-CD}+1.5Cu+TH588]^{2+}$, respectively (Fig. 1i). These findings not only provided direct evidence of γ-CD in CuTH@CD but also suggested a preliminary conclusion that the basic structural elements of CuTH@CD might involve coordination among three Cu^{2+}, two TH588 molecules, and two γ-CD molecules (Fig. 1j).

We then quantified the encapsulation rates of TH588 and Cu in CuTH@CD using ultraviolet-visible spectroscopy (UV–vis) and atomic absorption spectroscopy (AAS), determining rates of 32.8% and 14.7%, respectively (Figs. S3, S4a and b in Supporting information). Thus, the mole ratio of Cu to TH588 loaded in CuTH@CD NPs was about 1.5:1, indicating a high load capacity and excellent encapsulation efficiency that were favorable for subsequent experiments. Moreover, the pH-responsive release behavior of TH588 from CuTH@CD was observed. As depicted in Fig. 2a, the release equilibrium of TH588 by CuTH@CD in phosphate buffered saline (PBS) solution at different pH values was achieved within 12 h, with maximum cumulative release efficiencies reaching about 10% at pH 7.4, about 60% at pH 6.5, and about 80% at pH 5.5. This phenomenon might be attributed to the gradual protonation of γ-CD, weakening its coordination with both Cu^{2+} ions and TH588 as the environment shifts from neutral to weakly acidic conditions. Consequently, this leads to gradual nanoparticles disintegration and sustained low release of TH588. The results also demonstrated that CuTH@CD could dissociate in the acidic environment of the tumor, thereby enhancing its cytotoxic effect on tumor cells. In contrast, the weak dissociation observed in a neutral environment ensured its safety for normal tissues.

The successful fabrication of CuTH@CD motivated us to explore its diverse functions *in vitro*. Cu in the oxidized state within the nanoassembly directly interacts with and rapidly consumes GSH. Initially, we evaluated the GSH depletion ability of CuTH@CD using 5,5′-dithiobis-2-nitrobenoic acid (DTNB) as an indicator. As shown in Fig. S5 (Supporting information), increasing concentrations of CuTH@CD resulted in a fading of color and gradual rise in GSH consumption indicating that CuTH@CD could dissociate upon stimulation by GSH, leading to partial reduction of released Cu^{2+} to Cu^{+}. When the concentration of Cu reached 5.51×10^{-4} mg/mL, almost completely consumption of 1.0 mmol/L GSH was observed (the solution turned nearly clear and characteristic absorption at 412 nm almost disappeared) (Fig. 2b). As expected, CuTH@CD significantly promoted the GSH consumption, showing its great potential for enhanced CDT. To further confirm the Fenton-like activity of CuTH@CD, methylene blue (MB) was employed as an ·OH capture indicator, which undergoes oxidation by ·OH, resulting in a decreased UV absorption around 665 nm. Fig. 2c shows that under GSH stimulation, CuTH@CD NPs continuously and steadily released ·OH for up to 150 min until MB was completely faded, confirming the significant ·OH generation ability of CuTH@CD for CDT.

As GSH concentration gradually increased, we observed a non-linear relationship with ·OH production. Initially, ·OH generation increased with rising GSH levels, reaching a maximum at 1.0 mmol/L GSH. Beyond this concentration, ·OH production decreased. This trend was visually confirmed by corresponding changes in MB color (Fig. 2d and Fig. S6 in Supporting information). Moderate GSH concentrations optimally facilitate the dissociation of CuTH@CD, releasing Cu^{2+} that subsequently catalyze Fenton-like reactions to generate ·OH. Our findings demonstrate that CuTH@CD possesses the ability to consume GSH and generate ·OH, thereby amplifying oxidative damage for tumor therapy (Fig. 2e).

We evaluated the cellular internalization of the designed nanosystems in MCF-7 cells using Cy5-labeled CuTH@CD (Cy5-CuTH@CD). Confocal laser scanning microscopy (CLSM) images revealed an absence of obvious red fluorescence signals in cells treated with Cy5-CuTH, potentially attributable to its larger size and inadequate dispersity, which hindered effective phagocytosis (Fig. 3a). Conversely, treatment with CuTH@CD resulted in a significant enhancement of fluorescence signal, indicative of its remarkable cell penetration capability. Furthermore, after 4 h of treatment with PBS, CuTH, and CuTH@CD NPs, cellular uptake behavior was evaluated using flow cytometry (Fig. 3b and Fig. S7 in Supporting information). The fluorescence intensity observed in cells treated with CuTH@CD NPs surpassed that observed in those treated with CuTH NPs as consistent with CLSM results, thus confirming that γ-CD facilitated the formation of homogeneous and well-dispersed nanosystems. Subsequently, various cellular uptake inhibitors including chlorpromazine (CPZ), methyl-β-cyclodextrin (M-β-CD), and 5-(*N*-ethyl-*N*-isopropyl)-amiloride (EIPA) were employed to investigate the underlying endocytic mechanism. CPZ is a specific caveolin-mediated endocytosis inhibitor, M-β-CD can specifically inhibit caveolin-mediated endocytosis and EIPA is an inhibitor of macropinocytosis [51,52]. Flow cytometry assays revealed a significant inhibition of CuTH@CD endocytosis when cells were cultured with EIPA (Fig. 3c), indicating that micropinocytosis was the primary pathway for tumor cells internalization of CuTH@CD.

By virtue of efficient cellular uptake, the Cu-mediated ROS production was assessed *in vitro* against MCF-7 cells. We first eval-

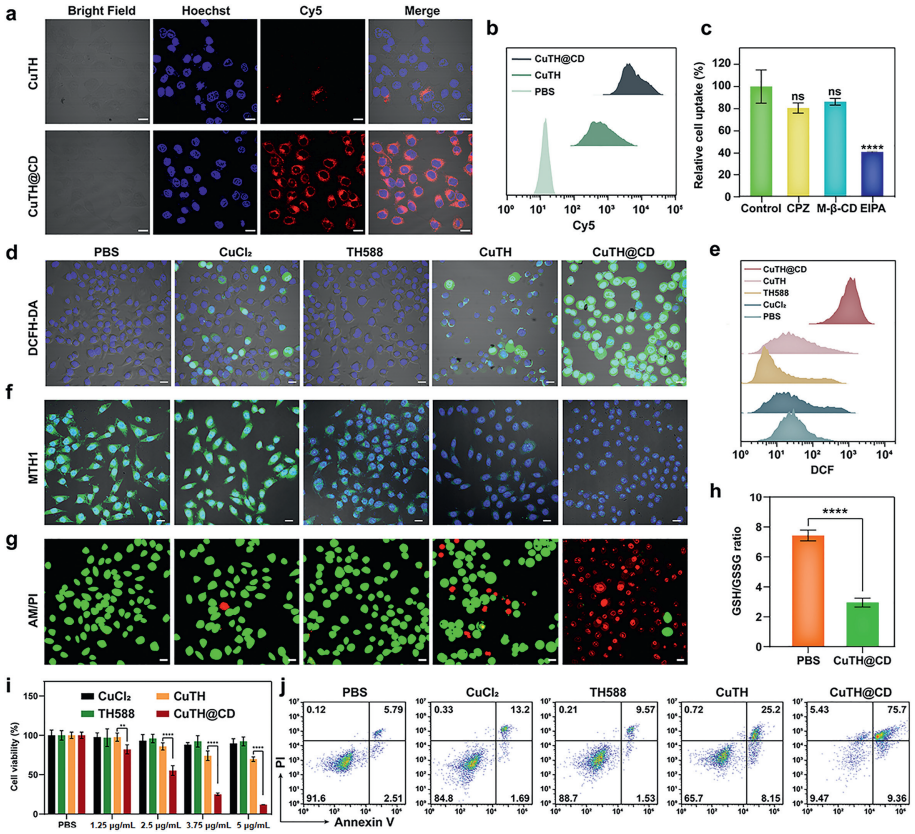

Fig. 3. Assessment of the antitumor efficacy *in vitro*. (a) CLSM images and (b) flow cytometry quantification of fluorescence intensity in MCF-7 cells after 4 h of incubation with CuTH or CuTH@CD NPs. Scale bar: 20 μm. (c) Endocytic mechanisms of CuTH@CD NPs ($n = 3$). (d) CLSM images and (e) flow cytometry quantification of MCF-7 cells treated with PBS, $CuCl_2$, TH588, CuTH and CuTH@CD, then stained with DCFH-DA. Scale bar: 40 μm. (f) Immunofluorescent staining images of MCF-7 cells treated with PBS, $CuCl_2$, TH588, CuTH and CuTH@CD for 4 h. Scale bar: 10 μm. (g) CLSM images of MCF-7 cells treated as indicated and then stained with calcein AM and propidium iodide. Scale bar: 20 μm. (h) GSH/GSSG ratio in MCF-7 cells with and without treatment of CuTH@CD. (i) Cell viability of MCF-7 cells treated with PBS, $CuCl_2$, TH588, CuTH and CuTH@CD ($n = 5$). (j) Flow cytometry detection of cell apoptosis induced by different treatments. Data are represented as means ± SD. $^{**}P < 0.01$, $^{****}P < 0.0001$ (one-way ANOVA). ns, no significance.

uated the intracellular Cu^+ levels. As shown in Fig. S8 (Supporting information), there was no significant difference in intracellular Cu^+ content between PBS and TH588 groups. A slight increase in intracellular Cu^+ was observed following treatment with $CuCl_2$ and CuTH, indicating that Cu^{2+} entered the cells reacted with GSH to produce Cu^+. Notably, the Cu^+ content in cells treated with CuTH@CD was significantly increased, demonstrating the release of Cu^+ from inside the nanosystem and the generation of Cu^+ following the reduction od Cu^{2+}. Besides, incubation with CuTH@CD NPs resulted in a decrease in the intracellular GSH/GSSG (glutathione, oxydized) ratio from approximately 7.43 to around 2.95 in MCF-7 cells (Fig. 3h), further demonstrated that GSH reduced Cu^{2+} within the NPs to Cu^+, subsequently down-regulating intracellular GSH levels and facilitating $^{\bullet}OH$ generation *via* Fenton-like reaction. We then evaluated the $^{\bullet}OH$ generating capacity of CuTH@CD NPs using an oxidative stress sensing probe 2′,7′-dichlorofluorescin diacetate (DCFH-DA) and a $^{\bullet}OH$ specific probe hydroxyphenyl fluorescein (HPF) through confocal fluorescence imaging and flow cytometry analysis. As illustrated in Figs. 3d and e and Fig. S9 (Supporting information), cells treated with CuTH@CD NPs exhibited significantly higher green fluorescence intensity compared to PBS and TH588 groups, indicating enhanced ROS generation mediated by Cu^+. Conversely, cells treated with both $CuCl_2$ and CuTH also showed partial fluorescence due to weaker Fenton-like reaction. HPF staining experiments also demonstrated a similar trend (Fig. S10 in Supporting information), confirming the excellent intracellular capacity of CuTH@CD for producing $^{\bullet}OH$.

To visually demonstrate the inhibitory effect of TH588-loaded NPs on MTH1 expression, immunofluorescence staining was employed to assess MTH1 accumulation in MCF-7 cells following different treatments. As shown in Fig. 3f and Fig. S11 (Supporting information), cells treated with TH588 and CuTH exhibited only a slight reduction in fluorescence intensity, due to limited endocytosis compared to the PBS and $CuCl_2$ groups. Conversely, the fluorescence signal in cells treated with CuTH@CD was significantly attenuated, indicating that the nanoassemblies effectively surpressed MTH1 expression.

To investigate the *in vitro* killing effect of CuTH@CD, we evaluated cell survival through cytotoxicity and flow apoptosis assays. The viability of MCF-7 cells treated with PBS, $CuCl_2$, TH588, CuTH and CuTH@CD NPs was assessed using the calcein AM/propidium iodide (PI) double-staining assay. As shown in Fig. 3g, treatment with CuTH@CD NPs induced significant cell death compared to the other groups where the killing effect was almost negligible. Furthermore, we examined the concentration-dependent cytotoxicity *via* cell counting kit-8 (CCK-8) assay and found that CuTH@CD NPs had a dose-dependent antitumor activity achieving up to 90% cell death rate at a concentration of 5 μg/mL (Fig. 3i). The potent antitumor activity of CuTH@CD NPs on MCF-7 cells was further confirmed by Annexin V-FITC/PI apoptosis detection assay (Fig. 3j), demonstrating its outstanding pro-oxidative damage effect on tumor cells. In addition, we assessed the oxidative damage in tumor cells by measuring the levels of 8–hydroxy-2 deoxyguanosine (8-OHdG), a biomarker for oxidative DNA damage. As shown in Fig. S12 (Supporting information), the intracellular level of

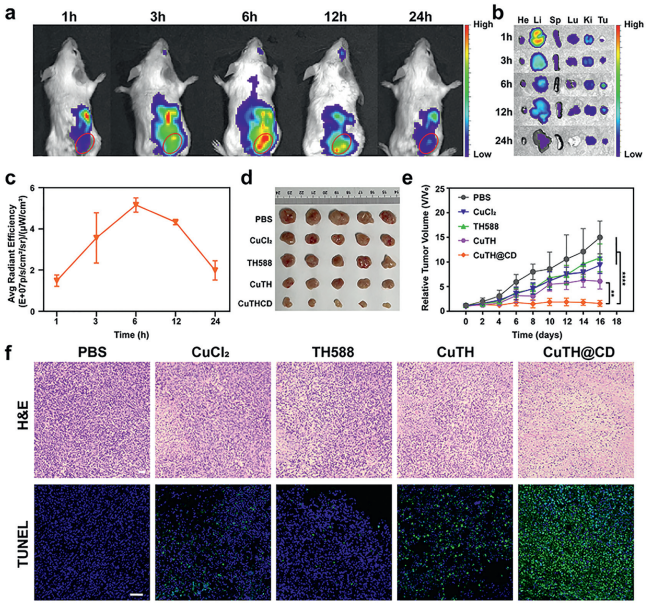

Fig. 4. Evaluation of the *in vivo* antitumor effect. (a) Whole-body fluorescence imaging of 4T1 tumor-bearing mice within 24 h injection of CuTH@CD. Red circles indicate tumor sites. (b) *Ex vivo* imaging of tumors and the major organs following administration of CuTH@CD. (c) Quantification of the fluorescence intensity at the tumor sites in (a). (d) Representative tumors isolated from 4T1 tumor-bearing mice after intravenous injection of PBS, $CuCl_2$, TH588, CuTH and CuTH@CD. (e) 4T1 tumor growth curves after different treatments. (f) H&E staining and TUNEL staining of tumor tissues from different treatment groups. Scale bar: 50 μm. Data are represented as means ± SD. ($n = 3$). $^{**}P < 0.01$, $^{****}P < 0.0001$ (one-way ANOVA).

8-OHdG was significantly increased following CuTH@CD treatment, indicating that CuTH@CD effectively inhibited the repair function of MTH1 on oxidative damage, thereby enhancing its cytotoxic effect on tumor cells.

Encouraged by the excellent properties of CuTH@CD NPs in enhancing oxidative damage *in vitro*, the efficiency of antitumor therapy was further evaluated *in vivo*. We assessed the tumor accumulation of CuTH@CD NPs in xenografted 4T1 tumor-bearing mice. Following intravenous injection of Cy5-CuTH@CD NPs, fluorescence signals at the tumor site rapidly increased and peaked at 6 h post-injection, followed by a subsequent decline from 6 to 24 h (Fig. 4a). Quantitative analysis revealed a significant enhancement in fluorescence intensity at the tumor site after 6 h of CuTH@CD NPs injection, which was approximately 3.47-, 1.45-, 1.19- and 2.60-fold higher than that observed at 1, 3, 12 and 24 h, respectively (Fig. 4c). In addition, *in vivo* imaging results were consistent with those obtained from imaging isolated tumors and normal organs (Fig. 4b, Figs. S13 and S14 in Supporting information), confirming effective accumulation of our nanoassembly at the tumor site post-administration in mice.

We further investigated the *in vivo* anti-tumor properties of CuTH@CD NPs using xenografted 4T1 tumor-bearing mice (all *in vivo* experiments were approved by the Institutional Animal Care and Use Committee of Beijing Tuberculosis and Thoracic Tumor Research Institute). Once the tumor volume reached about 80 mm^3, the mice were randomly divided into five groups ($n = 5$): PBS, $CuCl_2$, TH588, CuTH, and CuTH@CD. These groups received intravenous injections three times every other day. Throughout the treatment period, we monitored the tumor volume and body weight of each mouse every two days. As shown in Fig. 4c, PBS-treated mice exhibited rapid tumor growth, while those injected with $CuCl_2$, TH588, and CuTH NPs showed weak tumor growth inhibition. In contrast, significant inhibition of tumor growth was observed in mice treated with CuTH@CD NPs, indicating an excellent therapeutic effect resulting from the combination of Cu^{2+} and TH588 *in vivo*. Finally on day 16, mice were sacrificed, and their tumors were excised for photography and weighing, consistent with our previous data on tumor growth. (Figs. 4d and e, Fig. S15 in Supporting information). We further evaluated the expression of the MTH1 gene *in vivo* using quantitative real-time polymerase chain reaction (RT-qPCR). As shown in Fig. S16 (Supporting information), MTH1 gene expression in the tumor tissues of CuTH@CD-treated mice was significantly reduced, while the other control groups exhibited only a slight decreasing trend. This finding was consistent with the expression pattern of MTH1 protein in tumor cells. Additionally, hematoxylin and eosin staining (H&E) and terminal dUTP nick end labeling (TUNEL) of tumor tissue sections from CuTH@CD-treated mice revealed apparent nuclear dissociation and necrosis, confirming the potent anti-tumor therapeutic effect of CuTH@CD (Fig. 4f).

To assess the biosafety of CuTH@CD NPs for *in vivo* applications, we monitored mouse behavior and weight throughout the therapy period (Fig. S17 in Supporting information). No abnormal behavior or weight loss was observed, indicating minimal adverse effects at the administered doses. As shown in Fig. S18 (Supporting information), the hepatic function indexes such as alanine aminotransferase (ALT) and aspartate aminotransferase (AST), as well as the renal function parameters including blood urea nitrogen (BUN) and creatinine (CREA) were observed to be stable within reference ranges without conspicuous changes following the administration of CuTH@CD NPs. These findings confirmed that the designed CuTH@CD exhibited compatible hepatic and renal efficacy within this dosage range. Additionally, serum levels of the inflammatory cytokines interleukin-6 (IL-6) and IL-12 showed no significant differences, suggesting that CuTH@CD did not induce systematic inflammation *in vivo* (Fig. S19 in Supporting information). Complete blood counts fell within normal reference ranges (Fig. S20 in Supporting information), proving no manifestation of physical disorders or disease occurrence. Moreover, no evident pathological abnormalities in major normal organs (heart, liver, spleen, lung, and kidney) were observed across all groups tested by H&E staining (Fig. S21 in Supporting information), further demonstrating the favorable biosecurity profile when systemically administrating CuTH@CD NPs *in vivo*.

In summary, we have successfully developed a carrier-free nanoassembly (CuTH@CD) through supramolecular orchestration of γ-CD with Cu^{2+} and the MTH1 inhibitor TH588 for augmented oxidative damage in cancer therapy. The supramolecular regulation enabled the self-assembly of Cu^{2+}, TH588, and γ-CD into uniform-sized, well-dispersed nanoparticles at an optimal ratio of 3:2:2, achieving high drug loading content and stability without additional carriers. This design enhances cellular uptake and chemodynamic performance. Upon internalization, CuTH@CD releases Cu^{2+} to not only reduce the consumption of ROS by depleting GSH in tumor cells but also trigger the Fenton-like reaction to generate $^{\bullet}OH$ for CDT. Concurrently, released TH588 inhibits MTH1 activity, preventing DNA damage repair and further amplifying oxidative stress. This multi-pronged, synergistic approach enhances CDT efficiency by maximizing oxidative damage to tumor cells through increased ROS supply, inhibited ROS consumption, and amplified ROS effects, effectively invalidating tumor cell repair pathways. This work underscores the pivotal role of supramolecular chemistry in coordinating diverse functional components to construct integrated carrier-free delivery systems, thereby maximizing anti-tumor efficacy.

Declaration of competing interest

The authors declare that they have no known competing financial interests or personal relationships that could have appeared to influence the work reported in this paper.

CRediT authorship contribution statement

Xiaoyi Meng: Writing – original draft, Methodology, Investigation, Formal analysis. **Xinyue Sun:** Writing – original draft, Methodology, Investigation. **Zhaogang Sun:** Validation, Resources. **Yue Cheng:** Writing – review & editing, Funding acquisition, Conceptualization. **Yong Wang:** Validation, Resources. **Jun Ye:** Writing – review & editing, Supervision, Funding acquisition. **Yin Xiao:** Writing – review & editing, Supervision, Project administration. **Hongqian Chu:** Writing – review & editing, Supervision, Project administration, Funding acquisition, Conceptualization.

Acknowledgments

This work was financially funded by Tongzhou District Health Development Research Reserve Project Foundation (No. KJ2024CX024), Natural Science Foundation of Tianjin City (No. 23JCQNJC01640), National Natural Science Foundation of China (Nos. 82304393, 22404122), and Beijing Nova Program (No. Z211100002121127).

Supplementary materials

Supplementary material associated with this article can be found, in the online version, at doi:10.1016/j.cclet.2024.110765.

References

[1] G.S. Shadel, T.L. Horvath, Cell 163 (2015) 560–569.
[2] J.T. Liu, X.Y. Han, T.Y. Zhang, et al., J. Hematol. Oncol. 16 (2023) 116.
[3] E.C. Cheung, K.H. Vousden, Nat. Rev. Cancer 22 (2022) 280–297.
[4] B. Yang, Y. Chen, J.L. Shi, Chem. Rev. 119 (2019) 4881–4985.
[5] D. Kalyane, D. Choudhary, S. Polaka, et al., Prog. Mater. Sci. 130 (2022) 100974.
[6] K. Zhang, X.D. Meng, Z. Yang, H.F. Dong, X.J. Zhang, Biomaterials 258 (2020) 120278.
[7] X.Y. Meng, Z.G. Sun, H.Q. Chu, Y. Wang, Chem. Eng. J. 479 (2024) 147702.
[8] G. Chen, Y.Y. Yang, Q. Xu, et al., Nano Lett. 20 (2020) 8141–8150.
[9] B.C. Zhang, L. Lin, J.Z. Mao, et al., Chin. Chem. Lett. 34 (2023) 108518.
[10] Y.T. Zhong, Z.W. Qiu, Y.M. Li, et al., Chin. Chem. Lett. 36 (2025) 109846.
[11] X.L. Liu, X. Dong, S.C. Yang, et al., Adv. Sci. 8 (2021) 2003679.
[12] Z.P. Gao, S.Z. Zheng, K. Kamei, C.T. Tian, Acta Mater. Med. 1 (2022) 411–426.
[13] C. Wang, L.F. Chen, J.F. Zhu, et al., Adv. Funct. Mater. 34 (2024) 3332316092.
[14] S.J. Chen, T.L. Ma, J.H. Wang, et al., Biomaterials 305 (2024) 122456.
[15] X.Y. Zhong, X.W. Wang, J.X. Li, et al., Coord. Chem. Rev. 437 (2021) 213828.
[16] Q.Y. Zhang, Q.H. Luo, Z.M. Liu, M.C. Sun, X. Dong, Chem. Eng. J. 457 (2023) 141225.
[17] X.W. Wang, X.Y. Zhong, Z. Liu, L. Cheng, Nano Today 35 (2020) 100946.
[18] Y.Y. Yin, H. Wang, J.Q. Xue, et al., Adv. Healthc. Mater. 12 (2023) 2301269.
[19] M.X. Zhan, F.S. Wang, Y. Liu, et al., Adv. Sci. 10 (2023) 2207200.
[20] X.J. Di, Z.C. Pei, Y.X. Pei, T.D. James, Coord. Chem. Rev. 484 (2023) 215098.
[21] S.L. Li, P. Jiang, F.L. Jiang, Y. Liu, Adv. Funct. Mater. 31 (2021) 2100243.
[22] S.L. Li, X. Chu, H.L. Dong, H.Y. Hou, Y. Liu, Coord. Chem. Rev. 479 (2023) 215004.
[23] Y.J. Huang, Y.L. Jiang, Z.H. Xiao, et al., Chem. Eng. J. 380 (2020) 122369.
[24] M.M. Chen, S.J. Zhao, J.L. Zhu, et al., ACS Appl. Mater. Interfaces 14 (2022) 20682–20692.
[25] Y. Yuan, B. Chen, X.X. An, et al., Adv. Healthc. Mater. 13 (2024) 2304591.
[26] J.X. Yang, Y.C. Chuang, J.C. Tseng, et al., J. Exp. Clin. Cancer Res. 43 (2024) 169.
[27] K. Somyajit, R. Gupta, H. Sedlackova, et al., Science 358 (2017) 797–802.
[28] D. Dominissini, C. He, Nature 508 (2014) 191–192.
[29] L. Zhang, L. Misiara, G.J. Samaranayake, et al., Redox Biol. 40 (2021) 101848.
[30] G.J. Samaranayake, M. Huynh, P. Rai, Cancers 9 (2017) 47.
[31] Y.Z. Yina, F. Chen, Acta Pharm. Sin. B 10 (2020) 2259–2271.
[32] H. Gad, T. Koolmeister, A. Jemth, et al., Nature 508 (2014) 215–221.
[33] J.Y. Wang, L. Jin, X.G. Yan, et al., J. Invest. Dermatol. 136 (2016) 2277–2286.
[34] Y.T. Shao, M.M. Chen, W.L. Chen, et al., Adv. Healthc. Mater. 12 (2023) 2300503.
[35] J.J. Hu, Y. Chen, Z.H. Li, et al., Nano Lett. 19 (2019) 5568–5576.
[36] S.G. Rudd, H. Gad, K. Sanjiv, et al., Cancer Res. 80 (2020) 3530–3541.
[37] X.Y. Li, F.A. Deng, R.R. Zheng, et al., Small 17 (2021) 2102470.
[38] L.Z. Zhao, J.Y. Li, Y.Q. Su, et al., Sci. Adv. 6 (2020) eaaz0575.
[39] Q.C. Song, W.B. Yang, X.T. Deng, et al., Colloids Surf. B 218 (2022) 112715.
[40] Q.C. Song, Y.R. Zhang, X.T. Deng, et al., J. Mater. Chem. B 11 (2023) 3836.
[41] T. Zeng, W.J. Zang, H. Xiao, et al., ACS Nano 17 (2023) 18114–18127.
[42] N. Zhang, Z.J. Wang, G. Li, et al., Chem. Eng. J. 288 (2024) 150780.
[43] L.H. Liu, X.Z. Zhang, Prog. Mater. Sci. 125 (2022) 100919.
[44] H. Mei, S.S. Cai, D. Huang, et al., Bioact. Mater. 8 (2022) 220–240.
[45] L. Huang, S.J. Zhao, F. Fang, et al., Biomaterials 268 (2020) 120557.
[46] M.K. Shim, S. Yang, J. Park, et al., J. Nanobiotechnol. 20 (2022) 436.
[47] F.D. Arditti, D. Xu, D. Liu, et al., J. Clin. Oncol. 29 (2011) e13062.
[48] Y.M. Zhang, Y.H. Liu, Y. Liu, Adv. Mater. 32 (2019) 1806158.
[49] G. Decool, M. Kfoury, L. Paitel, A. Sardo, S. Fourmentin, Environ. Chem. Lett. 22 (2023) 321–353.
[50] H. Dossmann, L. Fontaine, T. Weisgerber, et al., Inorg. Chem. 60 (2021) 930–943.
[51] M.Y. Wu, H.B. Guo, L. Liu, Y. Liu, L.M. Xie, Int. J. Nanomedicine 14 (2019) 4247–4259.
[52] K. Ma, W.Z. Li, G. Zhu, et al., J. Drug Target 29 (2021) 884–891.